Computational screening of chalcogenides for intermediate band solar cells surpassing the Shockley–Queisser limit

PAPER • OPEN ACCESS

Computational screening of chalcogenides for intermediate band solar cells surpassing the Shockley–Queisser limit

To cite this article: Matteo Cagnoni 2025 *J. Phys. Energy* **7** 045010

Journal of Physics: Energy

PAPER

Computational screening of chalcogenides for intermediate band solar cells surpassing the Shockley–Queisser limit

Matteo Cagnoni

Politecnico di Torino, C.so Duca degli Abruzzi 24, 10129 Torino, Italy

E-mail: matteo.cagnoni@polito.it

Keywords: computational materials screening, electronic band structure, optoelectronic properties, intermediate band solar cells, principle of detailed balance

OPEN ACCESS

RECEIVED
7 April 2025

REVISED
27 June 2025

ACCEPTED FOR PUBLICATION
16 July 2025

PUBLISHED
5 August 2025

Abstract

Intermediate band solar cells offer a promising avenue to surpass the Shockley–Queisser limit of ∼30 % that constrains conventional single-junction devices, with the potential to approach an efficiency limit of ∼45 % in terrestrial environments by incorporating a metallic band within the valence-conduction gap. Yet, their practical realization is challenged by difficulties in developing suitable intermediate band (IB) materials. Current approaches, which involve adding inclusions or utilizing highly mismatched alloys, often degrade material quality or present significant technological hurdles. A possible solution that remains underexplored, is to identify crystalline materials that inherently possess an IB and fine-tune their properties. In this work, thousands of crystalline chalcogenides are analyzed using a detailed balance model to quantitatively evaluate their expected efficacy as IB materials. Notably, orthorhombic VB_1VIA_2 and IA_4VIA_6 compounds, such as Ta_1Se_2 and Cs_4S_6, are projected to achieve maximum efficiencies exceeding 35%, that is, surpassing the Shockley–Queisser limit. The interplay of IB filling and chemical substitution on the properties of these systems is analyzed, to unravel the impact on performance. This study not only identifies new material candidates for IB solar cells, but also provides insights into efficiency-property relations, hence advancing the understanding of these systems.

1. Introduction

The intermediate band (IB) solar cell is a promising concept to surpass the theoretical efficiency limit of single-junction devices based on the Shockley–Queisser model [1]. The latter rely on a conventional semiconductor to convert sunlight into free charge carriers, by absorbing photons with energy greater than the valence-conduction band gap. Because more carriers are photo-generated with a smaller band gap (higher current), but more energy is available from each carrier with a larger one (higher voltage), a trade-off exists that limits the maximum achievable power conversion efficiency to ∼30 % at 300 K under one Sun [2].

In IB solar cells, electronic states are introduced between the valence and conduction band of the photo-converting material [3], as shown in figure 1(a). These states serve as stepping stones, allowing valence electrons to reach the conduction band not only by absorbing a single photon with energy greater than the valence-conduction band gap, but also by sequentially absorbing two sub-gap photons. The first photon promotes the electron from the valence band (VB) to the IB, while the second photon moves it from the IB to the conduction band (CB). As a result, more charge carriers are photo-generated compared to conventional semiconductors, each one capable of supplying an amount of energy still equal to the valence-conduction band gap. Consequently, the current–voltage trade-off is significantly improved compared to Shockley–Queisser solar cells, effectively mimicking the behavior of complex multi-junction devices [4], but with a single material in the simple single-junction configuration.

Luque and Martí established the theoretical efficiency limit for IB solar cells using the principle of detailed balance [5]. By examining the optical coupling between each pair of bands through the resolved spectral absorbances A_{vi} (valence-intermediate), A_{ic} (intermediate-conduction), and A_{vc} (valence-conduction), they associated an electric current density with each band-to-band electronic transition. This

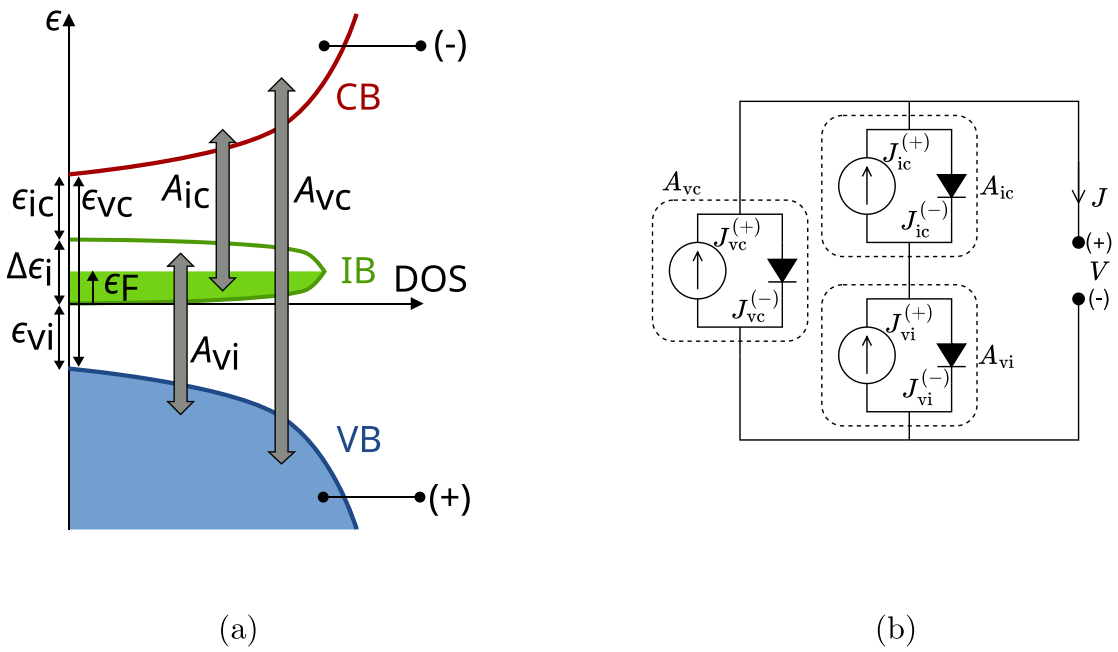

Figure 1. Working principle of intermediate band solar cells: (a) Electronic structure of the photo-converting material. (b) Equivalent circuit based on the principle of detailed balance.

includes currents induced by photon absorption ($J_{vi}^{(+)}$, $J_{ic}^{(+)}$, and $J_{vc}^{(+)}$), as well as those arising from the reverse process of photon emission ($J_{vi}^{(-)}$, $J_{ic}^{(-)}$, and $J_{vc}^{(-)}$). The interplay between these currents is depicted in the equivalent circuit [6] shown in figure 1(b), and determines the *JV* characteristic of the system.

With this model, the theoretical efficiency limit is ∼45 % at 300 K under one Sun, which is achieved with an infinitesimal IB width $\Delta\epsilon_i \approx 0$, a valence-intermediate band gap $\epsilon_{vi} \approx 0.9$ eV, an intermediate-conduction band gap $\epsilon_{ic} \approx 1.5$ eV, a valence-conduction band gap $\epsilon_{vc} \approx 2.4$ eV, and no spectral overlap between the aforementioned spectral absorbances. Additionally, the IB must be metallic, that is, the Fermi level ϵ_F must reside within it, for both incoming and outgoing electronic transitions to occur [7]. If this condition is not satisfied, one of the two sub-gap absorption channels is inhibited, causing complete compensation between photon absorption and emission in the other one. Then, the IB does not contribute to the output current and the device operates as a conventional Shockley–Queisser solar cell.

Unfortunately, the outstanding potential of IB solar cells remains largely untaped [8, 9]. With the highest efficiency reported to date of 18.7 % obtained with InAs quantum dots in a GaAs host [10], not even conventional Shockley–Queisser devices have been outperformed. A large portion of the blame lies in the significant challenges associated with obtaining IB materials that have optimal optoelectronic properties and charge transport capabilities.

In fact, the fabrication of these materials typically involves the incorporation of quantum dots [11] or dopant atoms [12, 13] into conventional semiconductors. GaAs is frequently employed as the host material; however, it exhibits sub-optimal optical properties. Specifically, GaAs has a band gap of ∼1.4 eV [14], which is significantly lower than the ideal valence-conduction band gap of ∼2.4 eV required for optimal IB operation under one Sun illumination. Moreover, the intermediate states created by these inclusions correspond to spatially localized electrons with energies situated near the midpoint of the valence-conduction band gap. These states serve as centers for non-radiative Shockley–Read–Hall recombination [15, 16], which can substantially diminish the performance of the device [17].

It has been argued that non-radiative Shockley–Read–Hall recombination can be inhibited by delocalizing the wave function of the intermediate states [18]. One potential approach to achieve this delocalization is through the Mott transition [19], which involves increasing the concentration of quantum dots or dopant atoms beyond the critical threshold above which the transition occurs. Unfortunately, the high concentrations needed to induce such transition typically lead to the formation of defects that degrade charge transport, or to an excessive broadening of the IB that negatively impacts optical properties [20].

To address the challenges associated with high concentrations of inclusions, the band anti-crossing model [21, 22] has been successively employed to create highly-mismatched alloys that feature an IB, such as GaN_xAs_{1-x}. These have been utilized in device prototypes [23]. Unfortunately, the significant mismatch between alloy components leads to large miscibility gaps that complicate both fabrication and property optimization, and induces strain in the material that adversely affects charge transport properties.

In the quest for materials featuring an IB of delocalized states with minimal degradation of optoelectronic and charge transport properties, a promising yet underexplored strategy involves utilizing intrinsic crystals that inherently possess an IB. This solution would ensure delocalization of the intermediate states and absence of performance-degrading defects.

To the best of the author's knowledge, only a limited number of studies have been published in the literature that investigate this pathway by computational materials science methods. First, Tablero and Wahnón [24] found that Ga_3P_4Ti crystals, obtained by substituting transition metals in super-cells of III–V semiconductors, exhibit a metallic IB. Later on, Padilha *et al* [25] realized that Magnéli phases of titanium dioxide (Ti_nO_{2n-1}) with well defined defect-free crystal structures form IBs by mimicking oxygen deficiency in TiO_2. Shortly after, Rasukkannu and coworkers [26–28] investigated a large number of ternary and quaternary crystalline materials, some of which exhibit an IB, such as Ag_2GeBaS_4, $Au_2Cs_2I_6$, and Ag_2KSbS_4. While these generally contain costly elements, such as Ag and Au, Liu *et al* [29] realized that the CB of kesterite I_2–II–IV–VI_4 quaternary chalcogenide semiconductors, already proposed as promising light absorbers for thin film solar cells, and their wurtzite counterparts, is isolated and can be viewed as an IB. Finally, Baquião and Dalpian [30] conducted a systematic screening of the AFLOW materials database [31]. They focused on crystalline materials and required for the IB to be not only present, but also metallic. This contrasts with previous studies, where the majority of materials exhibited empty IBs. From their screening, they identified $Bi_2Rh_2O_7$, $OsTb_6I_{10}$, and Ca_6FeN_5 as promising candidates.

Unfortunately, all of these efforts primarily concentrated on identifying the presence of an IB in the examined materials and assessing the proximity of the actual electronic band gaps and widths to their ideal values, without offering numerical estimates of the potential efficiency of devices that could utilize these materials.

In the work hereby presented, this knowledge gap is addressed by a quantitative assessment of the potential performance of a large number of chalcogenide materials as photo-converting agents in IB solar cells. Chalcogenide materials are very appealing for next generation photovoltaics because of their outstanding property tunability [32], typically low fabrication costs and complexities [33], and consolidated role in the current photovoltaics market [34]. The goal was to enhance the current understanding of intrinsic IB chalcogenide materials and facilitate the identification of those that show promise as photo-converting agents in IB solar cells.

The materials were analyzed by developing a simulation framework that relates the device power conversion efficiency with the filling of the intermediate band, while requiring only prior knowledge of the electron density of states. By considering the significant impact of such filling on the sub-gap spectral absorbances A_{vi} and A_{ic}, the potential of each material could be assessed more equitably, through a system ranking all potential candidates on the basis of the power conversion efficiency maximized not only with respect to the voltage (maximum-power-point), but also with respect to the Fermi level (optimal electron density). This appeared justified by the recognition that, in principle, the filling of the IB may be adjusted without necessarily increasing non-radiative Shockley–Read–Hall recombination, for example through shallow impurities [35]. At the same time, it guaranteed that no potentially high-performing materials were overlooked, including those that might only need minor adjustments to maximize their efficacy.

In the following sections, a comprehensive description of the methodology employed is provided, followed by a presentation of the results obtained from the aforementioned analysis:

(i) First, the final ranking of materials exhibiting the greatest potential is reported and discussed.
(ii) Next, a detailed analysis is conducted on two specific materials: orthorhombic Ta_1Se_2 (spacegroup Fmm2) and orthorhombic Cs_4S_6 (spacegroup $Cmc2_1$). These materials are chosen due to their exceptional predicted power conversion efficiency limits, exceeding 35 %, identified during the materials screening phase of this study. The impact of the Fermi level on their properties of interest and device performance is quantitatively studied.
(iii) Finally, the effects of iso-electronic chemical substitutions on the properties and performance of these two materials are examined. It is underscored that merely confirming the existence of an IB is insufficient; understanding the specifics of optical coupling is essential for achieving the desired performance.

2. Methods

2.1. Materials screening

In the first part of this study, the potential performance of a wide range of chalcogenide materials as photo-converting agents in IB solar cells was quantitatively assessed starting from their electron density of states.

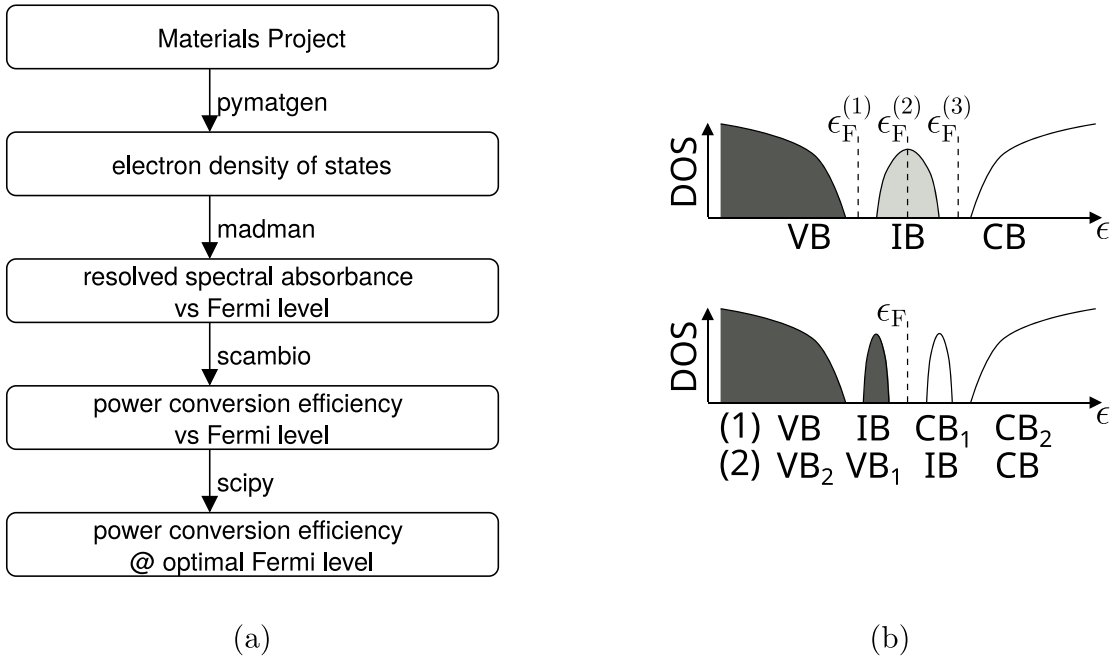

Figure 2. Overview of the methodology: (a) Workflow used to quantitatively assess the potential performance of each material. (b) Resolution of the electron density of states into bands according to the role of each band in an intermediate band solar cell.

The Materials Project database [36] served as the source for the electron density of states data. All available chalcogenide materials, that is, materials containing the elements sulfur S, selenium Se, or tellurium Te, were considered. At that time, the database contained a total of 24548 chalcogenide materials, with electron density of states data available for 13251 of them. Among these, 9498 materials featured an isolated band near the Fermi level, surrounded by a filled band and an empty band, that is, an electron density of states compatible with the electronic structure depicted in figure 1(a). The data was downloaded and pre-processed using the Python library `pymatgen` [37, 38] before carrying out further analysis. In particular, materials with an electron density of states spectrum exhibiting an energy resolution worse than 0.05 eV, or those showing inconsistent conduction types when derived from electronic band structure and electron density of states data, were discarded; the threshold of 0.05 eV was empirically established to obtain converged results from the detailed balance calculations conducted at 300 K. These precautions were taken to mitigate risks related to data quality that could compromise the validity of the conclusions drawn from the analysis.

Subsequently, the workflow illustrated in figure 2(a) was applied to each material to determine the power conversion efficiency of the corresponding IB solar cell at the maximum-power-point, as a function of the Fermi level and at optimal IB filling:

(i) First, the electron density of states was analyzed to identify energetically separated bands. These bands were categorized based on their potential roles in IB solar cells, following the classification illustrated in figure 1(a). In particular, a metallic band located between filled and empty bands was consistently classified as the IB. Additionally, a filled band situated just below the Fermi level or an empty band just above it—each surrounded by at least one additional filled band below and one additional empty band above—was also designated as an IB. Once the IB was identified, the filled bands below it were classified as VBs, while the empty bands above were categorized as CBs. This classification algorithm is depicted in figure 2(b).

(ii) Starting from the analysis above, the resolved spectral absorbances were determined as a function the Fermi level, according to the model outlined in section 2.2.

(iii) Then, the resolved spectral absorbances as a function of the Fermi level were utilized to calculate the dependence of the IB solar cell power conversion efficiency at maximum-power-point on the Fermi level itself. This was done by means of the detailed-balance model illustrated in section 2.3.

(iv) Finally, the Fermi level was optimized in order to maximize the power conversion efficiency at maximum-power-point of the IB solar cell.

The first two steps were conducted using the Python library `madman` (**MA**terial **D**ata **M**ining and **AN**alysis), while the third step utilized the `scambio` library (**S**olar **C**ell **A**nalysis **M**ade by **B**alancing photon **I**nput and **O**utput). Both libraries were developed by the author of this article and are accessible on Zenodo [39, 40]. In contrast, the final step involved optimization, which was performed using the `scipy` library [41]. All simulations were performed at 300 K, under one Sun illumination.

2.2. Resolved spectral absorbances

The spectral absorbances for the intermediate-intermediate (A_{ii}), valence-intermediate (A_{vi}), intermediate-conduction (A_{ic}), and valence-conduction (A_{vc}) electronic transitions were calculated based on the electron density of states (DOS_x) for the valence (x = v), intermediate (x = i), and conduction (x = c) bands.

For a given Fermi level ϵ_F and temperature T, the spectral densities of electrons and holes in band x were respectively expressed as [42]:

$$n_x(\epsilon;\epsilon_F,T) = DOS_x(\epsilon)\, f_{FD}(\epsilon;\epsilon_F,T) \tag{1}$$

$$p_x(\epsilon;\epsilon_F,T) = DOS_x(\epsilon)\,[1 - f_{FD}(\epsilon;\epsilon_F,T)] \tag{2}$$

where f_{FD} is the Fermi–Dirac distribution, given by:

$$f_{FD}(\epsilon;\epsilon_F,T) = \frac{1}{\exp\frac{\epsilon-\epsilon_F}{k_B T}+1}. \tag{3}$$

These were utilized to obtain the total density of electrons and holes:

$$n(\epsilon_F,T) = \sum_{x\in\{v,i,c\}} \int_{-\infty}^{+\infty} d\epsilon\, n_x(\epsilon;\epsilon_F,T) \tag{4}$$

$$p(\epsilon_F,T) = \sum_{x\in\{v,i,c\}} \int_{-\infty}^{+\infty} d\epsilon\, p_x(\epsilon;\epsilon_F,T). \tag{5}$$

Additionally, the joint density of states between bands x and y was defined as [43, 44]:

$$JDOS_{xy}(\hbar\omega;\epsilon_F,T) = \int_{-\infty}^{+\infty} d\epsilon\, n_x(\epsilon;\epsilon_F,T)\, p_y(\epsilon+\hbar\omega;\epsilon_F,T) \tag{6}$$

with $xy \in \{ii, vi, ic, vc\}$ and $\hbar\omega \geq 0$.

With this definition, the joint density of states incorporates the occupation of electronic states. To be non-zero, it requires not only the presence of pairs of states with an energy difference equal to $\hbar\omega$, but also that the lower energy states are occupied while the higher energy states are unoccupied. Consequently, the joint density of states quantifies the likelihood that a photon of energy $\hbar\omega$ is going to be absorbed by the material through an electronic transition.

Based on these considerations, the absorption coefficient between bands x and y was approximated as [45]:

$$\alpha_{xy}(\hbar\omega;\epsilon_F,T) = M\, JDOS_{xy}(\hbar\omega;\epsilon_F,T) \tag{7}$$

with M corresponding to an effective optical matrix element independent from xy.

The total joint density of states and absorption coefficient are simply [46]:

$$JDOS(\hbar\omega;\epsilon_F,T) = \sum_{xy\in\{ii,vi,ic,vc\}} JDOS_{xy}(\hbar\omega;\epsilon_F,T) \tag{8}$$

$$\alpha(\hbar\omega;\epsilon_F,T) = \sum_{xy\in\{ii,vi,ic,vc\}} \alpha_{xy}(\hbar\omega;\epsilon_F,T). \tag{9}$$

Finally, the resolved spectral absorbances were calculated as [47]:

$$\begin{aligned} A_{xy}(\hbar\omega;\epsilon_F,T) &= \frac{\alpha_{xy}(\hbar\omega;\epsilon_F,T)}{\alpha(\hbar\omega;\epsilon_F,T)} A(\hbar\omega;\epsilon_F,T) \\ &= \frac{JDOS_{xy}(\hbar\omega;\epsilon_F,T)}{JDOS(\hbar\omega;\epsilon_F,T)} A(\hbar\omega;\epsilon_F,T) \end{aligned} \tag{10}$$

where $A(\hbar\omega;\epsilon_F,T)$ is the total spectral absorbance at zero reflectance in the thick slab limit [48]:

$$A(\hbar\omega;\epsilon_F,T) = \lim_{d\to+\infty}\left\{1-\exp\left[\alpha(\hbar\omega;\epsilon_F,T)\,d\right]\right\}. \tag{11}$$

For the absorption channel xy, the absorption onset and offset were defined as the minimum and maximum photon energies $\hbar\omega_{xy}^{(on)}(\epsilon_F,T)$ and $\hbar\omega_{xy}^{(off)}(\epsilon_F,T)$, respectively, for which the corresponding spectral absorbance A_{xy} is non-zero.

Furthermore, each absorption channel was assigned a spectral weight and a spectral selectivity, respectively defined as:

$$W_{xy}(\epsilon_F,T) = \frac{\int_0^{+\infty}\mathrm{d}(\hbar\omega)\,A_{xy}(\hbar\omega;\epsilon_F,T)}{\int_0^{+\infty}\mathrm{d}(\hbar\omega)\,A(\hbar\omega;\epsilon_F,T)} \tag{12}$$

$$S_{xy}(\epsilon_F,T) = 1-\frac{\int_0^{+\infty}\mathrm{d}(\hbar\omega)\,A_{xy}(\hbar\omega;\epsilon_F,T)\,\left(A-A_{xy}\right)(\hbar\omega;\epsilon_F,T)}{\sqrt{\int_0^{+\infty}\mathrm{d}(\hbar\omega)\,A_{xy}^2(\hbar\omega;\epsilon_F,T)\int_0^{+\infty}\mathrm{d}(\hbar\omega)\,\left(A-A_{xy}\right)^2(\hbar\omega;\epsilon_F,T)}}. \tag{13}$$

These quantities quantify, respectively, the fraction of photons absorbed by the absorption channel in comparison with others, and the extent to which the absorption channel spectrally overlaps with others.

2.3. Power conversion efficiency

The maximum-power-point efficiency of IB solar cells utilizing the material under study was determined using the principle of detailed balance, along with the resolved spectral absorbances introduced in section 2.2. It was assumed that these absorbances, obtained for the material at the equilibrium, are not significantly affected by changes in the charge carrier population within each band during operation. This assumption was justified by the focus on unconcentrated sunlight, for which it holds true, as discussed in the previously published literature [49].

The model employed is a slight generalization of the framework proposed by Levy and Honsberg [50], which builds upon the foundational work of Luque and Martí (discussed in section 1) by incorporating an IB with a finite width ($\Delta\epsilon_i > 0$). This consideration is particularly important for crystalline materials, where the IB consists of delocalized states. Such states are expected to undergo broadening due to chemical bonding, making the inclusion of a finite width essential for accurately modeling the material's performance.

Levy and Honsberg associated an optical absorption onset and offset with each absorption channel, as defined in section 2.2. In cases where competing channels exist at a given photon energy, they assumed that the channel with the highest onset dominates, which implies no spectral overlap between different absorption channels. Consequently, they assigned a spectral absorbance of 1 to the dominant active channel and a value of 0 to the others, resulting in a resolved absorption spectrum similar to that shown in Figure 3(a).

Their study provides valuable insights into optimizing IB materials for solar cells, which can be extracted from figure 3(b). For $\hbar\omega_{vc}^{(on)} < 3\,\mathrm{eV}$, an infinitesimal IB is expected to yield optimal performance, as hypothesized by Luque and Martí. Because of the infinitesimal IB width, the optical absorption onsets and offsets coincide with the electronic band gaps. As $\hbar\omega_{vc}^{(on)}$ increases, a wider IB helps protect against performance degradation. Ultimately, for $\hbar\omega_{vc}^{(on)} > 4\,\mathrm{eV}$, the IB should be maximally wide; its optimum might even exceed $\hbar\omega_{vi}^{(on)}$ in models allowing spectral overlap. At 300 K under one Sun, the best efficiency is achieved when $\hbar\omega_{ii}^{(off)} = 0$, $\hbar\omega_{vi}^{(on)} = 0.9\,\mathrm{eV}$, $\hbar\omega_{ic}^{(on)} = 1.5\,\mathrm{eV}$, and $\hbar\omega_{vc}^{(on)} = 2.4\,\mathrm{eV}$.

In this work, the resolved spectral absorbances from Levy and Honsberg were replaced with those defined in section 2.2. This approach offers some advantages over the original model:

- It lifts the condition of no spectral overlap between different channels.
- It explicitly accounts for the spectral weight of each channel.
- It explicitly considers the impact of the Fermi level and temperature.

These adjustments allowed for a more accurate assessment of each material's potential to meet the IB paradigm, enabling fairer comparisons among materials without relying on computationally intensive methods.

The foundation of every detailed-balance model is the photon flux density per unit energy emitted by a blackbody at temperature T and radiation chemical potential μ, given by the generalized Planck's law [51]:

$$\dot{n}_{BB}(\hbar\omega;\mu,T) = \frac{2\pi}{c^2h^3}(\hbar\omega)^2 f_{BE}(\hbar\omega;\mu,T) \tag{14}$$

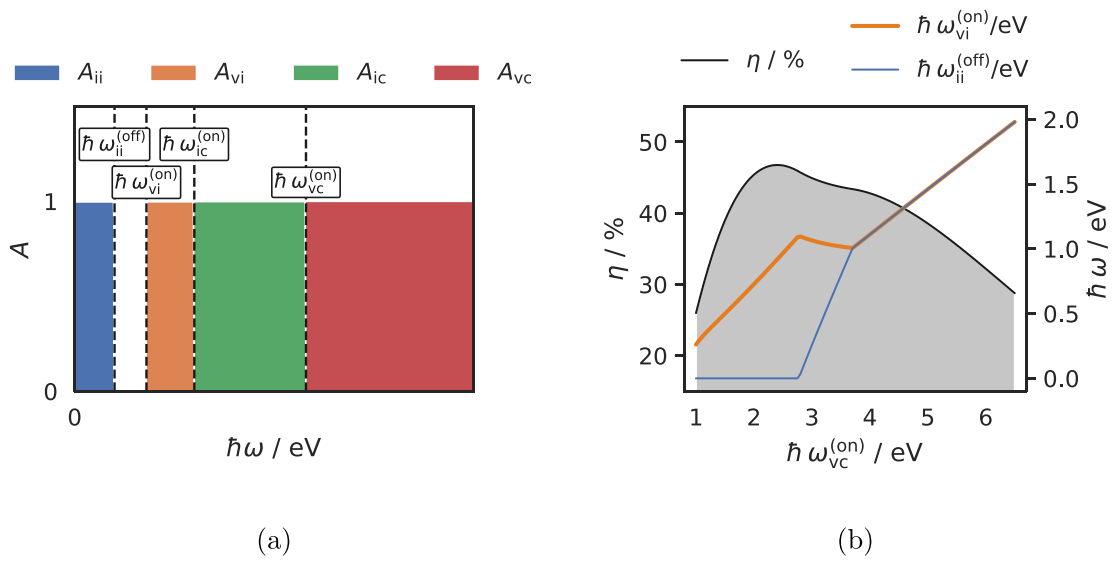

Figure 3. Model of Levy and Honsberg: (a) Resolved spectral absorbances. (b) Optimized power conversion efficiency, valence-intermediate optical absorption onset, and intermediate-intermediate optical absorption offset as a function of the valence-conduction optical absorption onset, at 300 K under one Sun.

where f_{BE} is the Bose–Einstein distribution:

$$f_{BE}\left(\hbar\omega;\mu,T\right)=\frac{1}{\exp\left(\frac{\hbar\omega-\mu}{k_B T}\right)-1}. \tag{15}$$

By modeling the Sun as a blackbody at temperature $T_{Sun}=6000\,K$ and radiation chemical potential $\mu_{Sun}=0$, the photon flux density absorbed by the IB material through the xy absorption channel was calculated as:

$$\dot{N}_{xy}^{(+)}\left(\epsilon_F,T\right)=C_{cell}\,C_{Sun}\int_0^{+\infty}\mathrm{d}\left(\hbar\omega\right)A_{xy}\left(\hbar\omega;\epsilon_F,T\right)\dot{n}_{BB}\left(\hbar\omega;\mu_{Sun},T_{Sun}\right) \tag{16}$$

where $C_{Sun}=\left(R_{Sun}/\mathrm{a.u.}\right)^2\approx 46000^{-1}$ is sunlight's attenuation factor at Earth's surface, C_{cell} ($=1$ for unconcentrated sunlight) is the solar cell concentration factor [52], and ϵ_F and T are the equilibrium Fermi level and operating temperature of the IB material.

At the same time, since the spectral emissivity equals the spectral absorbance according to Kirchhoff's law of radiation [53], the photon flux density emitted by the IB material through the xy channel was computed as:

$$\dot{N}_{xy}^{(-)}\left(\mu_{xy};\epsilon_F,T\right)=\int_0^{+\infty}\mathrm{d}\left(\hbar\omega\right)A_{xy}\left(\hbar\omega;\epsilon_F,T\right)\dot{n}_{BB}\left(\hbar\omega;\mu_{xy},T\right) \tag{17}$$

where μ_{xy} is the radiation chemical potential of the xy electronic transitions.

These photon flux densities were directly related to the electric current densities depicted in the equivalent circuit of figure 1(b) according to:

$$\begin{aligned}J_{xy}\left(\mu_{xy};\epsilon_F,T\right)&=J_{xy}^{(+)}\left(\epsilon_F,T\right)-J_{xy}^{(-)}\left(\mu_{xy};\epsilon_F,T\right)\\&=q\dot{N}_{xy}^{(+)}\left(\epsilon_F,T\right)-q\dot{N}_{xy}^{(-)}\left(\mu_{xy};\epsilon_F,T\right)\end{aligned} \tag{18}$$

where q is the elementary charge.

Then, the solar cell current density J was determined as a function of the voltage V by calculating the radiation chemical potentials associated with each photon exchange channel.

First, due to the design of the IB being electrically insulated, the electric current densities corresponding to valence-intermediate and intermediate-conduction electronic transitions must be equal:

$$J_{vi}\left(\mu_{vi}\left(V\right);\epsilon_F,T\right)=J_{ic}\left(qV-\mu_{vi}\left(V\right);\epsilon_F,T\right). \tag{19}$$

In this equation, the intermediate-conduction radiation chemical potential μ_{ic} is expressed as $qV - \mu_{vi}$. This relationship arises from the fact that the conduction and valence bands serve as the respective contacts for extracting photo-generated electrons and re-injecting them into the device upon energy transfer to the end user. Thus, $qV = \mu_{vc} = \mu_{vi} + \mu_{ic}$.

After determining $\mu_{vi}(V)$, the solar cell current density was simply obtained as:

$$J(V;\epsilon_F,T) = J_{vc}\left(qV;\epsilon_F,T\right) + J_{vi}\left(\mu_{vi}\left(V\right);\epsilon_F,T\right) \tag{20}$$

Finally, the solar cell maximum-power-point efficiency was evaluated as:

$$\eta(\epsilon_F,T) = \frac{100}{P_{Sun}} \max_V \{J(V;\epsilon_F,T)\ V\} \tag{21}$$

where $P_{Sun} = C_{Sun}\,\sigma\,T_{Sun}^4$, with σ equal to Stefan Boltzmann's constant.

The analysis presented offered an evaluation of the potential efficiency of an IB solar cell, determined solely from the material's electron density of states as a function of the equilibrium Fermi level ϵ_F and temperature T. By optimizing the efficiency with respect to the Fermi level, the maximum achievable efficiency was identified for each material, independent of extrinsic effects such as sub-optimal doping. This approach revealed the true potential of each material, along with the optimal values for quantities such as electron density and spectral absorbances.

2.4. DFT calculations

Following the completion of the screening phase, during which many materials were evaluated for their potential performance in IB solar cells, a detailed analysis was conducted on orthorhombic Ta_1Se_2 (spacegroup Fmm2) and orthorhombic Cs_4S_6 (spacegroup $Cmc2_1$), along with iso-structural and iso-electronic materials. This analysis aimed to enhance the understanding of the interplay between IB filling and relevant properties, as well as how these properties can be tuned through chemical substitution.

For these materials, the electron density of states was recalculated to improve data quality. Specifically, the following steps were undertaken for each material:

(i) Data from the Materials Project was utilized for the initial atomic structure.
(ii) The atomic structure was relaxed to its equilibrium configuration by minimizing the total energy with respect to atomic coordinates and unit cell vectors.
(iii) The corresponding ground state electron density was calculated.
(iv) Starting from the ground state electron density, the electronic band structure and electron density of states were computed, including a sufficient number of empty bands, to verify the presence of an intermediate band and assess its conducting nature (metallic or insulating).

These calculations were performed using density functional theory (DFT) [54] in conjunction with the Projector Augmented Wave (PAW) method [55]. The Atomistic Simulation Environment (`ase`) [56] was employed alongside `gpaw` [57] for the calculations. `gpaw`'s pseudo-potentials were used to model the electron-nuclei interactions, while the Perdew–Burke–Ernzerhof (PBE) functional [58] was applied for exchange and correlation. Single-electron wave functions were expanded using a plane wave basis set, with a small smearing applied to metallic systems to enhance convergence. Convergence with respect to the plane wave energy cutoff and the density of the **k**-point grid was verified under strict criteria. Structural relaxation was performed until all forces were reduced to below 0.01 eV $Å^{-1}$.

The routines employed in these calculations were included in the aforementioned Python library `madman`.

3. Results and discussion

3.1. Materials screening

Table 1 reports the top candidates as photo-converting materials in IB solar cells at 300 K under one Sun, based on the materials screening campaign conducted. In particular, it displays Materials Project identifier (MPID), unit cell chemical formula, lattice system, IB filling at the intrinsic Fermi Level $\epsilon_F^{(0)}$, valence-conduction band gap ϵ_{vc}, IB width $\Delta\epsilon_i$ and maximum-power-point efficiency η at the optimal Fermi level ϵ_F^*. To ensure clarity and focus on the most promising solutions, the full dataset, which is going to be made available on Zenodo [59] and may be the first one to systematically report a quantitative evaluation of the power conversion efficiency limit of several materials for IB solar cells, was filtered according to the following criteria:

Table 1. Materials Project identifier, unit cell chemical formula, lattice system, intermediate band filling at the intrinsic Fermi Level, valence-conduction band gap, intermediate band width and maximum-power-point efficiency at the optimal Fermi level of the top candidates as photo-converting materials in intermediate band solar cells at 300 K under one Sun.

MPID	Formula	Lattice	Filling(i)	ϵ_{vc}/eV	$\Delta\epsilon_i$/eV	$\eta(\epsilon_F^*)$/%
mp-8954	Ta_1Se_2	orthorhombic	metallic	3.0	1.2	37.4
mp-558 762	$K_1Sn_1S_2$	trigonal	metallic	3.1	1.1	35.0
mp-999 267	$Rb_1Sn_1S_2$	trigonal	metallic	3.0	1.2	34.6
mp-7795	$Rb_1Sn_1S_2$	trigonal	metallic	3.1	1.2	34.5
mp-7794	$K_1Sn_1S_2$	trigonal	metallic	3.2	1.1	34.0
mp-1874	Nb_1S_2	hexagonal	metallic	2.9	1.2	33.0
mp-1072 712	Nb_2S_4	hexagonal	metallic	2.8	1.3	32.8
mp-1013 525	V_2S_4	hexagonal	metallic	2.0	1.1	32.6
mp-571 016	$K_2Sn_2Se_4$	tetragonal	metallic	2.6	1.6	32.4
mp-27 682	$Na_1Sn_1S_2$	trigonal	metallic	3.3	1.5	31.9
mp-1072 086	Ta_2S_4	hexagonal	metallic	3.3	1.5	31.2
mp-8719	$K_4Mn_2Te_4$	orthorhombic	metallic	2.7	1.5	30.9
mp-1984	Ta_2S_4	hexagonal	metallic	3.1	1.8	30.9
mp-1411	Ta_1S_2	orthorhombic	metallic	3.3	1.4	30.8
mp-10 014	Ta_1S_2	trigonal	metallic	3.1	1.8	30.7
mp-573 947	$Cs_4Mn_2Se_4$	orthorhombic	metallic	2.6	1.5	30.0
mp-1079 600	Cs_4S_6	orthorhombic	filled	2.4	0.3	41.1
mp-239	Ba_2S_6	tetragonal	filled	2.5	0.8	40.8
mp-7446	Rb_4S_6	orthorhombic	filled	2.3	0.4	37.8
mp-7667	K_4S_6	orthorhombic	filled	2.2	0.5	36.8
mp-7547	Ba_2Se_4	monoclinic	filled	2.4	1.3	33.9
mp-505 634	Cs_4Te_6	orthorhombic	filled	2.4	1.4	31.5
mp-7447	Rb_4Se_6	orthorhombic	filled	3.3	1.6	30.5
mp-570 589	Se_4Br_4	orthorhombic	empty	3.0	1.2	40.5
mp-8361	Cs_4Te_4	orthorhombic	empty	2.2	0.6	34.8
mp-1170	Sn_1S_2	trigonal	empty	3.8	1.4	33.2
mp-665	Sn_1Se_2	trigonal	empty	3.0	1.6	32.9
mp-8360	Rb_4Te_4	orthorhombic	empty	2.1	0.8	32.8
mp-28 099	S_4Br_4	orthorhombic	empty	4.3	0.6	32.0

- Only materials exceeding the Shockley–Queisser limit of ∼30 % are reported.
- The valence-conduction band gap was restricted to values between 1 and 6 eV, where the Shockley–Queisser limit is surpassed in the model by Levy and Honsberg (figure 3(b)).
- For the same reason, the valence-intermediate band gap was limited to values greater than 0.2 eV. Because of the symmetry of the model of Levy and Honsberg with respect to the exchange of valence-intermediate and intermediate-conduction, the same restriction was applied to the intermediate-conduction band gap.
- Materials with simpler structures were favored by limiting the number of elements and atoms per unit cells, because: 1) fewer elements reduce the possible combinations of decomposition products, thereby decreasing the likelihood of instability; 2) simpler materials, with fewer atoms per unit cell, are easier to study, model, and optimize. This restriction is anticipated to facilitate the identification of stable, high-quality IB materials that can be reliably fabricated and fine-tuned, hence increasing the likelihood of successful outcomes in future experimental research. This was translated into restricting the attention to materials with a maximum of three distinct elements if the IB was metallic, a maximum of two distinct elements if the IB was insulating, and a maximum of ten atoms per unit cell in both cases.
- Only materials that are either thermodynamically stable or experimentally observed were included to ensure that practical realization is feasible.

Table 1 indicates that only a limited number of sufficiently simple materials can surpass the Shockley–Queisser limit. Merely possessing an IB is not enough; if the corresponding absorption properties cannot be optimized to approach the archetype established by Levy and Honsberg (figure 3(a)), the overall performance will remain low even with adjustments to the Fermi level. However, this should not be discouraging, as the practical realization of high-performing IB solar cells—an innovation that could be truly transformative for the next generation of solar technologies—requires only one functioning material.

Notably, all top candidates possess hexagonal, orthorhombic, or trigonal crystal structures, suggesting that these configurations may be favorable for achieving an optimal IB electronic structure. The leading materials are consistently orthorhombic, regardless of the intrinsic IB filling. This observation may serve as a new guideline for the identification of new IB materials.

Table 2. Materials Project identifier, unit cell chemical formula, and valence-intermediate and intermediate-conduction absorption onsets and spectral selectivities, at the optimal Fermi level, of the top candidates as photo-converting materials in intermediate band solar cells at 300 K under one Sun.

MPID	Formula	$\hbar\omega_{\mathrm{vi}}^{(\mathrm{on})}(\epsilon_{\mathrm{F}}^{*})$/eV	$\hbar\omega_{\mathrm{ic}}^{(\mathrm{on})}(\epsilon_{\mathrm{F}}^{*})$/eV	$S_{\mathrm{ii}}(\epsilon_{\mathrm{F}}^{*})$	$S_{\mathrm{vi}}(\epsilon_{\mathrm{F}}^{*})$	$S_{\mathrm{ic}}(\epsilon_{\mathrm{F}}^{*})$	$S_{\mathrm{vc}}(\epsilon_{\mathrm{F}}^{*})$
mp-8954	Ta_1Se_2	0.97	1.42	1.00	0.92	0.71	0.81
mp-558 762	$K_1Sn_1S_2$	1.11	1.22	1.00	0.77	0.55	0.80
mp-999 267	$Rb_1Sn_1S_2$	1.12	1.11	1.00	0.78	0.57	0.82
mp-7795	$Rb_1Sn_1S_2$	1.11	1.12	1.00	0.78	0.58	0.83
mp-7794	$K_1Sn_1S_2$	1.11	1.17	1.00	0.77	0.56	0.81
mp-1874	Nb_1S_2	1.01	1.23	1.00	0.88	0.67	0.80
mp-1072 712	Nb_2S_4	0.98	1.12	1.00	0.86	0.74	0.86
mp-1013 525	V_2S_4	0.45	0.77	0.99	0.83	0.61	0.75
mp-571 016	$K_2Sn_2Se_4$	1.01	0.96	1.00	0.69	0.46	0.82
mp-27 682	$Na_1Sn_1S_2$	1.31	1.27	1.00	0.73	0.61	0.86
mp-1072 086	Ta_2S_4	1.24	1.32	1.00	0.83	0.73	0.86
mp-8719	$K_4Mn_2Te_4$	1.25	0.86	0.99	0.78	0.49	0.74
mp-1984	Ta_2S_4	1.08	1.31	0.99	0.83	0.74	0.86
mp-1411	Ta_1S_2	1.25	1.36	1.00	0.84	0.67	0.81
mp-10 014	Ta_1S_2	1.05	1.30	0.99	0.82	0.67	0.80
mp-573 947	$Cs_4Mn_2Se_4$	1.26	0.86	1.00	0.69	0.43	0.67
mp-1079 600	Cs_4S_6	0.81	1.34	1.00	0.96	0.72	0.78
mp-239	Ba_2S_6	0.60	1.44	1.00	0.97	0.74	0.79
mp-7446	Rb_4S_6	0.60	1.34	1.00	0.96	0.67	0.75
mp-7667	K_4S_6	0.42	1.31	1.00	0.96	0.64	0.73
mp-7547	Ba_2Se_4	0.95	0.81	1.00	0.77	0.50	0.69
mp-505 634	Cs_4Te_6	0.96	0.82	0.99	0.62	0.56	0.58
mp-7447	Rb_4Se_6	1.34	1.30	1.00	0.70	0.49	0.61
mp-570 589	Se_4Br_4	1.52	0.94	1.00	0.75	0.91	0.79
mp-8361	Cs_4Te_4	0.99	0.63	1.00	0.85	0.82	0.94
mp-1170	Sn_1S_2	1.57	1.30	1.00	0.75	0.73	0.84
mp-665	Sn_1Se_2	1.33	0.96	0.99	0.70	0.53	0.80
mp-8360	Rb_4Te_4	0.83	0.61	1.00	0.78	0.75	0.91
mp-28 099	S_4Br_4	2.23	1.48	1.00	0.85	0.91	0.85

While Fermi level optimization in metallic systems can benefit from the presence of an already metallic IB, the wider IBs in these systems may lead to performance degradation at optimal valence-conduction band gaps. The best-performing metals notably exhibit valence-conduction band gaps that exceed the ideal value of 2.4 eV, corresponding to the region in the plot based on the model by Levy and Honsberg (figure 3(b)), where wider IBs are associated with higher solar cell efficiency. The scarcity of narrow band metals is consistent with the tendency of such materials to transition to an insulating state due to Coulomb repulsion among electrons. This phenomenon results in the splitting of the metallic band into two insulating bands—one filled and one empty—consistent with the Mott-Hubbard metal–insulator transition model [60]. Consequently, finding materials that are both intrinsically metallic and narrow band may prove to be quite challenging. Among the selected materials, only one exceeded 35.0 % efficiency: orthorhombic Ta_1Se_2 with spacegroup Fmm2.

As a result, insulating systems that can be converted to metallic states through reasonable doping with shallow impurities—without significantly increasing non-radiative Shockley–Read–Hall recombination—may be better suited to match ideal absorption properties and achieve ultra-high performance; this partly differs from the requirement of intrinsically metallic IB adopted by Baquião and Dalpian in their computational screening study [30]. This is supported by the observation that the highest efficiencies ($\geqslant$40 %) are found in materials with either filled or empty IBs. These insulating materials exhibit significantly narrower IBs, aligning the optimal valence-conduction band gap region with the maximum achievable efficiency predicted by Luque and Martí. The best ones exhibit a valence-conduction band gap very close the ideal
value of 2.4 eV.

Additional considerations can be made by considering the optical absorption onsets and spectral selectivities introduced in section 2.2 reported in table 2 for optimal Fermi level values. $\hbar\omega_{\mathrm{ii}}^{\mathrm{off}}(\epsilon_{\mathrm{F}}^{*})$ and $\hbar\omega_{\mathrm{vc}}^{\mathrm{on}}(\epsilon_{\mathrm{F}}^{*})$ are not reported, because they basically coincide with $\Delta\epsilon_{\mathrm{i}}$ and ϵ_{vc} at 300 K under one Sun; these are already displayed in table 1.

As expected, the best-performing materials are those that closely approach the ideal values of not only the previously discussed ϵ_{vc} (2.4 eV) and $\Delta\epsilon_{\mathrm{i}}$ (0), but also $\hbar\omega_{\mathrm{vi}}^{\mathrm{on}}$ (0.9 eV) and $\hbar\omega_{\mathrm{ic}}^{\mathrm{on}}$ (1.5 eV). Additionally, they are

the ones with spectral selectivity values closer to 1, indicating minimal spectral overlap between different absorption channels. This reinforces the significance of the spectral selectivity quantifier.

Among the reported materials, orthorhombic Ta_1Se_2 (spacegroup Fmm2) and orthorhombic Cs_4S_6 (spacegroup $Cmc2_1$) emerged as particularly promising candidates based on their respective maximum efficiencies of 37.4 % and 41.1 %, and ideal representatives of metallic and insulating systems for a more in depth analysis. To the best of the author's knowledge, this is the first time that they are proposed as IB materials for solar cells, and, beside the aforementioned Magnéli phases derived from titanium dioxide [25], may represent the first examples of very promising binary compounds. The impact of the IB filling on their properties and performance is discussed in the next section.

According to the Materials Project, both materials have been experimentally observed. Notably, orthorhombic Cs_4S_6 is predicted to be thermodynamically stable and was successfully fabricated through the reaction of pure Cs with S [61]. In contrast, orthorhombic Ta_1Se_2 is not predicted to be thermodynamically stable, and its experimental realization necessitated the intercalation of misfit layers [62, 63]. For practical applications, it will be essential to also address the air stability of these materials, which, if missing, could be achieved by compositional tuning or barrier layers, as done for perovskites for solar cells [64].

These experimental challenges are deemed worth pursuing, as the predicted efficiency limits above 35 % are significantly higher than the current record efficiency of 18.7 % [10] reported for intermediate band solar cells. This suggests that the potential of this technology remains largely unexplored. Additionally, these materials could serve as archetypes to elucidate the structure-property relationships that lead to IB behavior, thereby facilitating the identification of new promising materials.

3.2. Impact of IB filling: orthorhombic Ta_1Se_2 and Cs_4S_6

Figure 4 displays the electronic band structures and electron densities of states of orthorhombic Ta_1Se_2 (spacegroup Fmm2) and orthorhombic Cs_4S_6 (spacegroup $Cmc2_1$), computed with high accuracy as outlined in section 2.4.

As already discussed, Ta_1Se_2 is intrinsically metallic, with the Fermi level crossing the relatively wide IB. In contrast, Cs_4S_6 is intrinsically insulating. The highest group of filled bands was identified as the IB following the algorithm outlined in section 2.1 and illustrated in figure 2(b). This IB is significantly narrower than that of Ta_1Se_2, which is expected to facilitate a closer alignment with the ideal absorption properties defined by Luque and Martí and corroborated by Levy and Honsberg.

The resolved spectral absorbances as a function of the Fermi level were computed for both materials according to the methodology presented in section 2.2. The results for intrinsic and optimized values of the Fermi level are displayed in figure 5, and compared with the ideal optical absorption onsets and offsets defined by Levy and Honsberg.

In its intrinsic state, Cs_4S_6 is unable to exchange photons through electronic transitions between the intermediate and conduction bands, or via intra-band transitions within the IB, due to the complete filling of the IB (see figure 5(b)). Consequently, the intermediate-conduction current densities, $J_{ic}^{(+)}$ and $J_{ic}^{(-)}$, are both zero. As discussed in section 1, the continuity of electric current density, combined with the intentional electrical insulation of the IB, leads to a situation where the photon absorption and emission processes between the valence and IBs fully compensate each other. Thus, $J_{vi}^{(+)} = J_{vi}^{(-)}$, and the device operates as a conventional Shockley–Queisser solar cell, relying solely on electronic transitions between the valence and conduction bands. As a result, the maximum-power-point efficiency is expected to be low.

In contrast, Ta_1Se_2 features a metallic intermediate band in its intrinsic state. With the IB being partially filled, all photon exchange channels are active, allowing the cell to function as an IB solar cell (see figure 5(a)). However, the relatively broad IB results in the optical absorption onsets and offsets being significantly displaced from the ideal values, as indicated by the dashed lines in the figures. Therefore, while the maximum-power-point efficiency can be anticipated to be somewhat higher than that of intrinsic Cs_4S_6, it remains low.

Upon optimizing the Fermi level, the spectral absorbance of Ta_1Se_2 can be adjusted to better align with the ideal targets, as illustrated by the comparison between figures 5(a) and (c). Unfortunately, the absorbance still does not reach the ideal targets, and although the maximum-power-point efficiency improves, it is unlikely to fully realize the potential of IB solar cells.

Conversely, in the case of Cs_4S_6, the optical absorption onsets and offsets become remarkably close to the ideal targets following Fermi level optimization, suggesting a significantly improved maximum-power-point efficiency.

Unfortunately, in both materials, there exists substantial spectral overlap between the intermediate-conduction and valence-conduction absorbances. This overlap is a critical performance detractor, preventing the efficiency from reaching the ideal value of 45 % predicted for perfect spectral separation, even for Cs_4S_6.

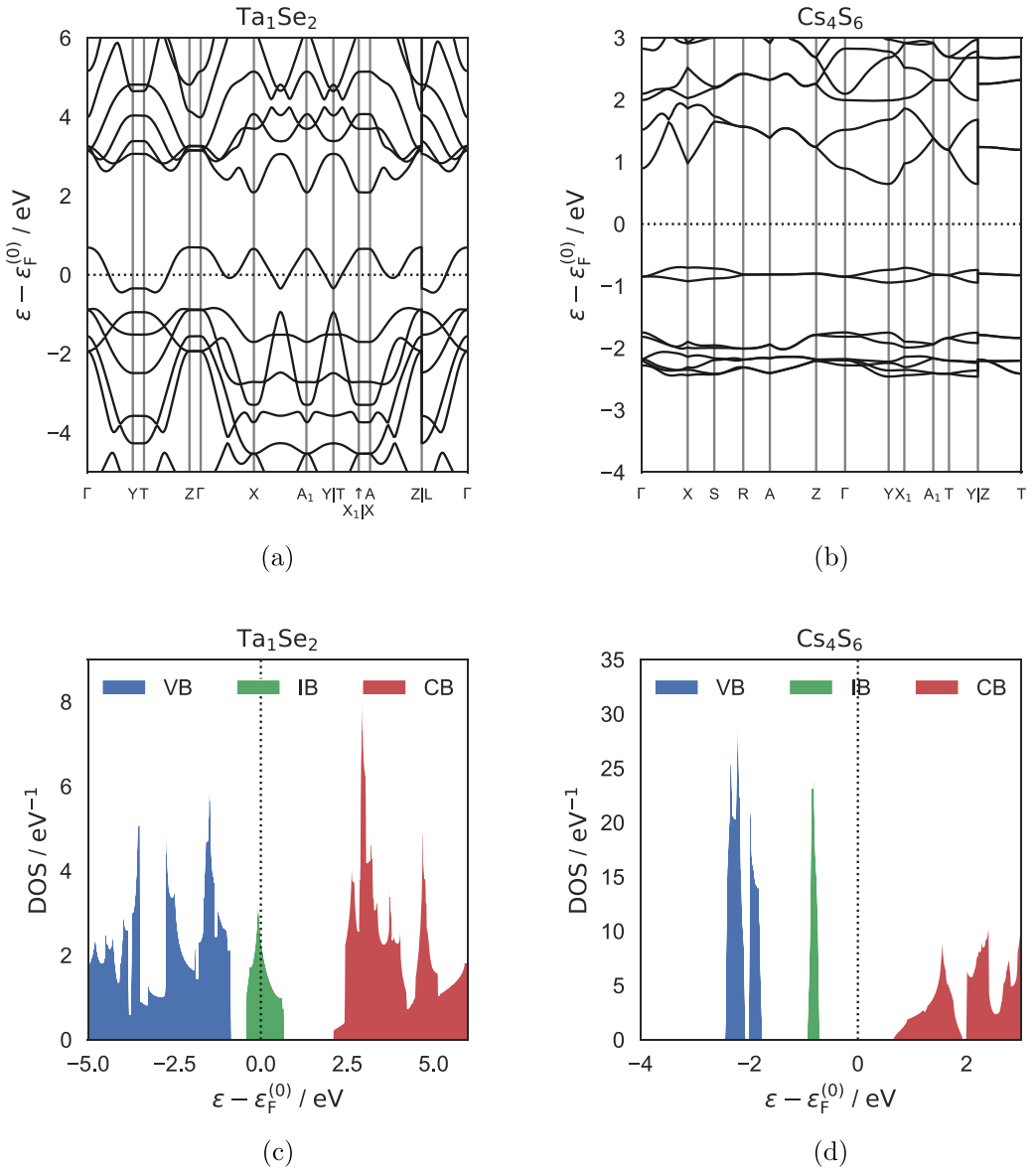

Figure 4. Electronic properties of orthorhombic Ta_1Se_2 and Cs_4S_6: (a)–(b) Electronic band structures. (c)–(d) Electron densities of states.

These observations are substantiated in figure 6, where the maximum-power-point efficiency η and electron density variation $\Delta n(\epsilon_F) = n(\epsilon_F, T) - n(\epsilon_F^{(0)}, T)$ are plotted as a function of the Fermi level variation $\Delta\epsilon_F = \epsilon_F - \epsilon_F^{(0)}$ for both materials.

Interestingly, the electron density adjustment required in Ta_1Se_2, $\Delta n(\epsilon_F^*) \approx 7.18 \times 10^{21}\,\mathrm{cm}^{-3}$, is greater than that needed in Cs_4S_6, $\Delta n(\epsilon_F^*) \approx -5.80 \times 10^{20}\,\mathrm{cm}^{-3}$, to optimize the Fermi level. This diminishes the advantage of Ta_1Se_2, which features a metallic IB in its intrinsic state, compared to Cs_4S_6, which exhibits a filled IB in its intrinsic state, and further supports the counter-intuitive statement made above that intrinsically metallic systems might not be the best option. Because its optimal Fermi level lies very close to the upper edge of the IB, achieving the desired electron density in Cs_4S_6 may necessitate a slight reduction in the number of electrons to transition it into a degenerate semiconductor. Similar electron densities have been observed in other chalcogenide materials, such as the ones used in thermoelectric applications, often due to the spontaneous formation of cation vacancies [65]. For these, also adjustments in carrier concentration through dopant atoms, as opposed to vacancies, have been extensively studied in the literature [66]. This systematic understanding may facilitate the development of effective doping strategies also for IB chalcogenide materials to achieve the desired spectral absorbance characteristics.

As noted, the optimal Fermi level of Cs_4S_6 is situated very close to the band edge. This proximity arises from the energy difference between the VB maximum and the IB maximum, which closely aligns with the

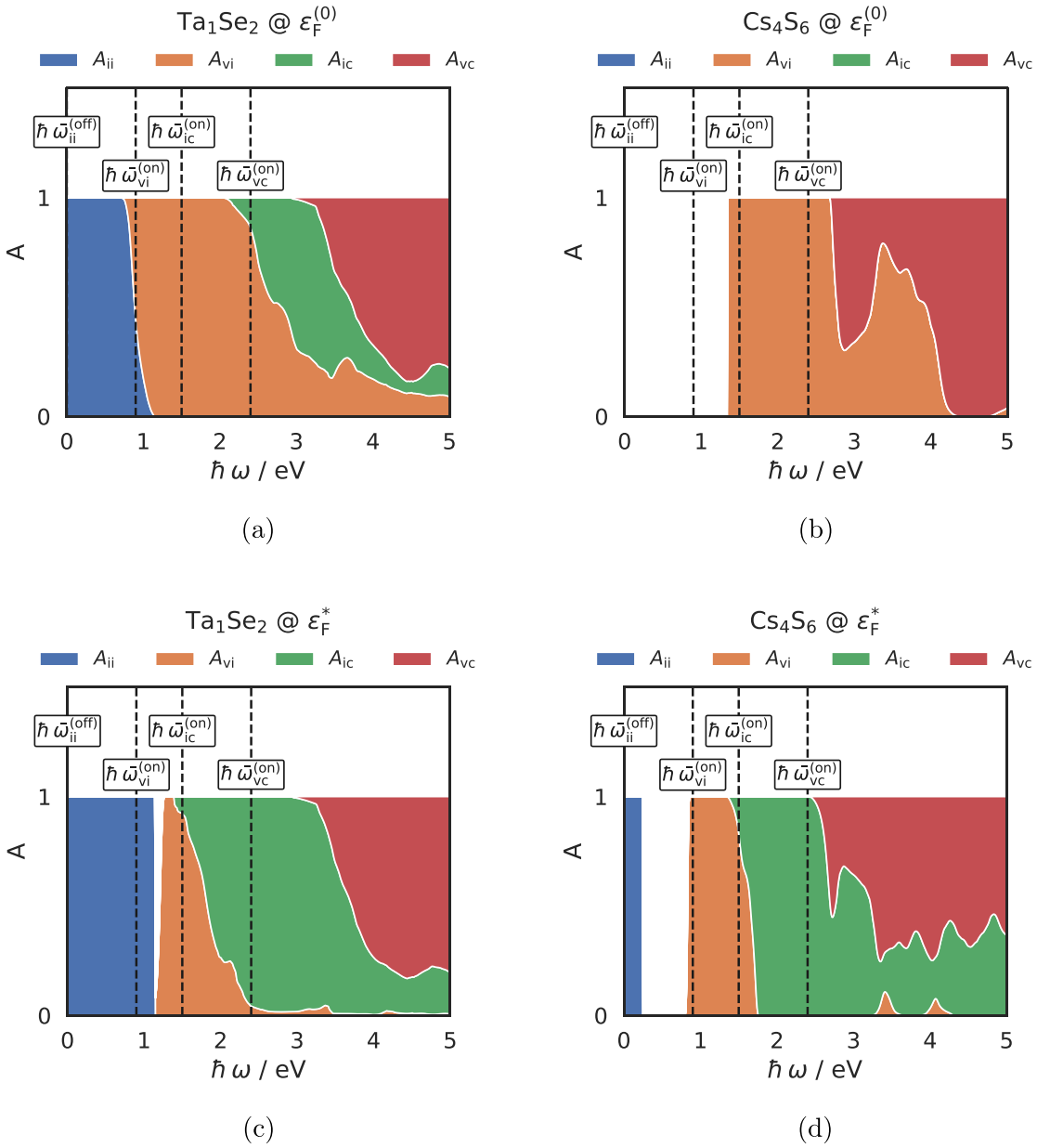

Figure 5. Optical absorption properties of orthorhombic Ta_1Se_2 and Cs_4S_6: (a)–(b) Intrinsic resolved spectral absorbances. (c)–(d) Optimized resolved spectral absorbances. These are compared with the ideal values for the optical absorption onsets, which are marked by dashed vertical lines.

ideal onset for valence-intermediate optical absorption. Consequently, facilitating transitions from the VB to just the upper edge of the IB promotes a closer approach to this ideal valence-intermediate absorption onset.

It is important to remark that detailed balance models do not incorporate charge transport properties such as carrier mobility (assumed infinite). Based on the electronic band structures reported in figures 4(a) and (b), the effective masses of VB holes and CB electrons are not expected to be particularly light for both Ta_1Se_2 and Cs_4S_6. This indicates that extraction of photo-generated charge carriers may be inefficient for a very thick absorbing layer [67]. This could be circumvented by utilizing thin films of these materials, which would in turn require preservation of high absorbance by intrinsically strong optical absorption or light trapping strategies that increase the effective optical absorption length [68].

Regarding the recombination of photo-generated charge carriers, the detailed balance model presented operates under the radiative limit, considering only radiative recombination processes. This approach is justified by the delocalization of IB states, which is a characteristic feature of crystalline materials possessing intrinsic IBs. This delocalization effectively suppresses Shockley–Read–Hall non-radiative recombination [18], a process that typically leads to significant degradation of charge transport properties in solar cells where the IB is formed through the incorporation of localized electronic states. Consequently, non-radiative recombination was assumed to be negligible.

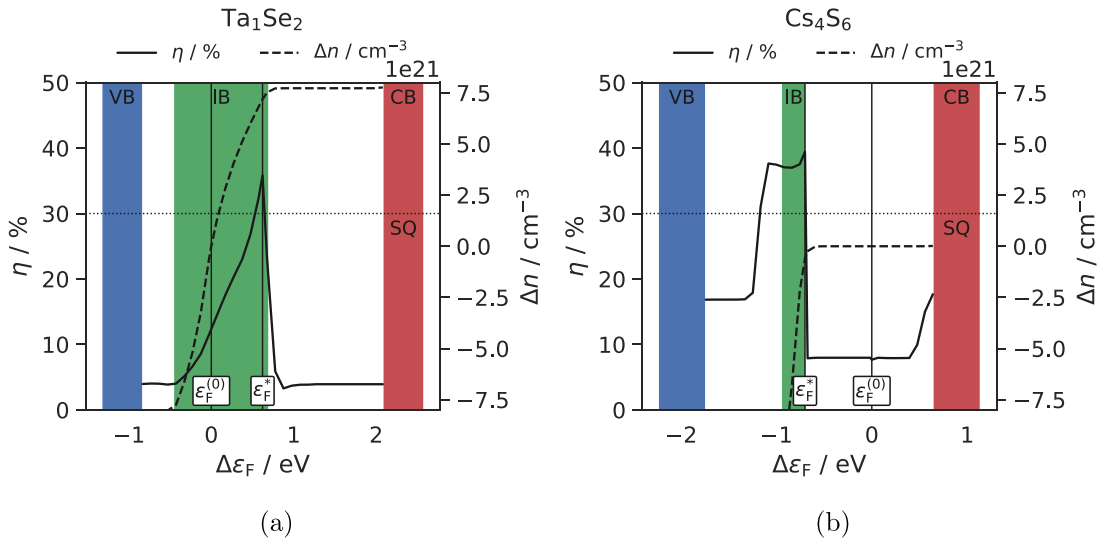

Figure 6. Maximum-power-point efficiency calculated at 300 K under one Sun, and electron density variation, as a function of the Fermi level: (a) Ta_1Se_2. (b) Cs_4S_6.

Table 3. Unit cell chemical formula, maximum-power-point efficiency, valence-conduction band gap, intermediate band width, valence-intermediate and intermediate-conduction absorption onsets, and spectral selectivities, at the optimal Fermi level, of the orthorhombic VB_1VIA_2 and IA_4VIA_6 compounds studied, calculated at 300 K under one Sun.

Formula	$\eta(\epsilon_F^*)/\%$	ϵ_{vc}/eV	$\Delta\epsilon_i$/eV	$\hbar\omega_{vi}^{(on)}(\epsilon_F^*)$/eV	$\hbar\omega_{ic}^{(on)}(\epsilon_F^*)$/eV	$S_{ii}(\epsilon_F^*)$	$S_{vi}(\epsilon_F^*)$	$S_{ic}(\epsilon_F^*)$	$S_{vc}(\epsilon_F^*)$
Ta_1Se_2	35.8	2.9	1.2	1.0	1.4	1.0	0.9	0.8	0.9
Nb_1S_2	32.0	2.8	1.2	1.0	1.2	1.0	0.8	0.8	0.9
Ta_1S_2	30.7	3.3	1.4	1.2	1.3	1.0	0.8	0.8	0.9
Nb_1Se_2	–	–	–	–	–	–	–	–	–
Cs_4S_6	39.0	2.4	0.3	0.8	1.3	1.0	1.0	0.8	0.8
Rb_4S_6	36.4	2.2	0.3	0.6	1.3	1.0	1.0	0.8	0.8
Cs_4Te_6	30.3	2.4	1.4	1.0	0.8	1.0	0.7	0.6	0.8
Cs_4Se_6	28.6	1.4	0.3	0.3	0.8	1.0	0.9	0.8	0.8
K_4Se_6	28.1	3.2	1.8	1.4	1.2	1.0	0.7	0.6	0.8
K_4S_6	27.5	2.1	0.4	0.4	1.3	1.0	0.9	0.8	0.9
Rb_4Se_6	20.5	1.1	0.4	0.0	0.7	1.0	0.9	0.6	0.8

3.3. Impact of electronic band structure: orthorhombic VB_1VIA_2 and IA_4VIA_6 compounds

Finally, the impact of iso-electronic chemical substitution on the properties and performance of Ta_1Se_2 and Cs_4S_6 was examined by investigating other orthorhombic VB_1VIA_2 and IA_4VIA_6 compounds using the previously discussed methodology. This approach allowed for a comprehensive assessment of how the electronic band structure affects properties and performance at optimal Fermi levels, while also exploring potential enhancements through techniques such as alloying.

Table 3 presents the unit cell chemical formula, maximum-power-point efficiency, valence-conduction band gap, IB width, valence-intermediate and intermediate-conduction absorption onsets, and spectral selectivities, at the optimal Fermi level, for the orthorhombic VB_1VIA_2 and IA_4VIA_6 compounds studied. As before, these values were calculated at 300 K under one Sun. The ones for Ta_1Se_2 and Cs_4S_6 differ slightly from those reported in tables 1 and 2, as the latter were derived from the electron densities of states available in the Materials Project database, while the former are based on DFT calculations conducted in this study.

Ta_1Se_2 and Cs_4S_6 were confirmed as the best candidates within their respective material classes. Interestingly, despite the optimization of the Fermi level, performance can significantly degrade in other compositions. For instance, Cs_4Se_6, K_4Se_6, K_4S_6, and Rb_4Se_6, although iso-electronic and iso-structural to Cs_4S_6, exhibit maximum-power-point efficiencies below 30 % at the optimal Fermi level. A similar trend is observed in VB_1VIA_2 compounds, where a more drastic effect occurs: in Nb_1Se_2, the IB overlaps with the VBs, resulting in the loss of the IB electronic structure. Consequently, no quantitative data is reported for this material in table 3. This behavior can be attributed to increasing deviations from ideal optical absorption onsets and reduced spectral selectivities in materials projected to have poorer performance. These observations confirm that, in addition to the critical role of IB filling discussed in section 3.2, the specific features of the electronic band structure - particularly the position and width of the bands—are crucial in

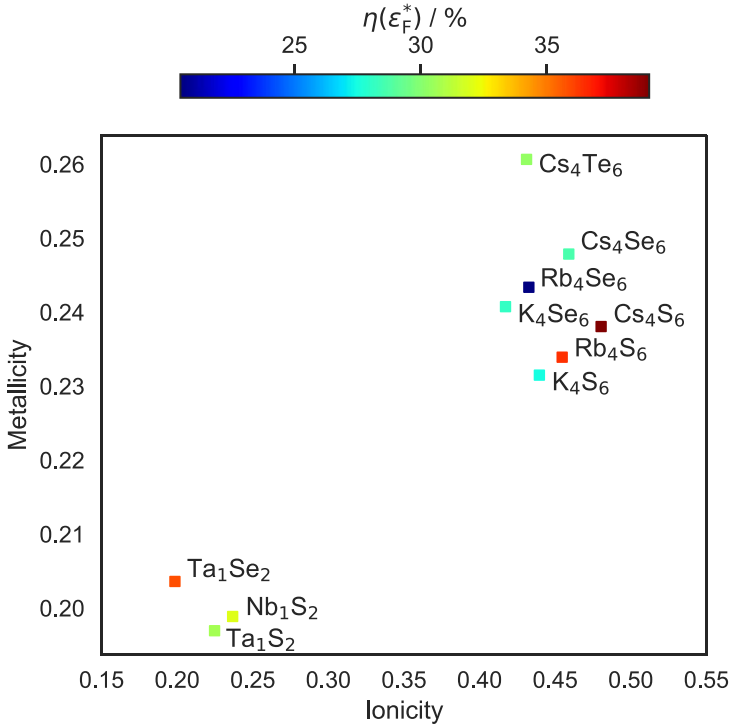

Figure 7. Maximum-power-point efficiency at the optimal Fermi level as a function of the material's ionicity and metallicity, calculated at 300 K under one Sun.

determining the final performance. Therefore, it is insufficient to merely confirm the presence of an IB, and at least a quantitative assessment using detailed balance methods is warranted due to its efficiency.

To effectively visualize the performance degradation induced by iso-electronic substitutions, figure 7 displays the maximum-power-point efficiency at the optimal Fermi level as a function of the material's metallicity and ionicity, calculated at 300 K under one Sun. As for table 3, Nb_1Se_2 is not displayed because it does not feature an IB electronic structure.

Such material maps are valuable tools for illustrating the interplay between properties and atomic structure or chemical bond properties, and for identifying systematics, as discussed in previous works on other material systems [69–73]. Therefore, they can assist in finding optimal alloys or new materials.

The ionicity and metallicity of a $X_m Y_n$ compound were defined as [74, 75]:

$$\text{Ionicity} = \left|\frac{\chi_X - \chi_Y}{\chi_X + \chi_Y}\right| \tag{22}$$

$$\text{Metallicity} = \frac{2}{\chi_X + \chi_Y} \tag{23}$$

where χ_X and χ_Y are the Mulliken's electronegativities [76] of the constituent elements X and Y, derived from `pymatgen`'s data.

Clearly, only a limited number of compositions achieve a maximum-power-point efficiency above 35 % at the optimal Fermi level, namely Ta_1Se_2, Cs_4S_6, and Rb_4S_6. This highlights the significance of not only adjusting electron density but also finely tuning the electronic band structure to fully leverage the potential of the IB paradigm.

4. Conclusion and outlook

Chalcogenides are attractive for next-generation photovoltaics due to their tunable properties, low fabrication costs, and established market presence. Furthermore, materials with intrinsic IBs could address challenges associated with current solutions, which are based on inclusions or atomic-mismatch that degrade material quality or create technological hurdles. Therefore, thousands of crystalline chalcogenide materials from the Materials Project database were analyzed for their potential as photo-converting materials in IB solar cells.

A methodological improvement was made in screening intrinsic IB materials, by focusing on quantifying the potential efficiency rather than merely identifying the presence of an IB. By explicitly accounting for the

impact of the IB filling on the optical absorption properties, and for the spectral weights and selectivities of the different absorption channels, a more accurate assessment of the potential of each material was enabled. This ensured that no potentially high-performing materials were overlooked, especially those that may require minor adjustments for optimal efficacy.

Several promising material classes for the IB paradigm were identified, such as orthorhombic VB_1VIA_2 and IA_4VIA_6 compounds. Within these, Ta_1Se_2 and Cs_4S_6 were projected to exceed a 35 % maximum efficiency at 300 K under one Sun, surpassing the Shockley–Queisser limit. Cs_4S_6 is particularly noteworthy, as it may approach a 40 % efficiency limit, with its elements being Earth abundant [77]. Given their potential, these two classes were studied more in detail, with focus on the interplay of materials properties and performance with IB filling and chemical substitution.

More generally, the systematic study revealed that all promising materials with simple structures exhibit hexagonal, orthorhombic, or trigonal configurations, with the best performers consistently being orthorhombic. At the same time, it was concluded that an intrinsically metallic IB is not necessarily advantageous; for instance, the electron density adjustment required for optimal performance was higher in the metallic Ta_1Se_2 compared to the insulating Cs_4S_6. Additionally, top-performing metallic systems were observed to have broader IBs, while promising insulating materials were associated with narrower bands, warranting further investigation into the optimal pathways to approach the ideal target of a metallic IB of infinitesimal width. Finally, the relatively low fraction of IB materials actually exceeding a 30 % efficiency limit underscored the importance of closely matching the electronic structure and optical absorption targets defined by Luque and Martí, and by Levy and Honsberg, through their respective detailed balance models. The limited number of promising materials should not pose a concern, as only one effective solution is needed for IB solar cells. However, integration into device architecture will necessitate optimization of various additional aspects, such as contacts and anti-reflection coatings, alongside potential challenges related to the materials themselves.

The adoption of the PBE exchange-correlation functional is a notable limitation of this study, because it systematically underestimates material band gaps [78]. Furthermore, estimation of the spectral weights of different absorption channels based solely on the joint density of states may lead to inaccuracies. Unfortunately, more precise methods, such as hybrid functionals or GW for the electronic band structure, and the Bethe–Salpeter equation for the absorption coefficients [79], would have required extensive recalculations of too many materials, which was computationally prohibitive within this work; for example, the computational cost of a GW calculation was estimated to be on average 1000 times greater than that of the corresponding PBE calculation [80]. Nevertheless, previous computational studies on IB materials showed that the PBE exchange-correlation functional is qualitatively reliable for the identification of IBs, because it preserves the overall band structure except for band gap sizes [26, 29]. Fortunately, the ability to tune properties through alloying is expected to enable compensation for computational systematic errors at the experimental level. Furthermore, this study aimed to provide insights rather than definitive material recipes, particularly through the identification of promising material classes and their common traits, and a general quantification of the impact of IB filling and electronic structure details on the potential solar cell performance. Thus, the adopted methodology was deemed adequate for its intended purpose.

It is hoped that this study will inspire further research to validate the findings, explore better materials, or propose novel high-performing devices, leveraging the potential of chalcogenide materials to realize the intermediate band solar cell concept.

Data availability statement

The data cannot be made publicly available upon publication because they are not available in a format that is sufficiently accessible or reusable by other researchers. The data that support the findings of this study are available upon reasonable request from the authors.

Acknowledgments

The work has been carried out as part of the project *PhANTOM*, funded by the Italian Ministry of University and Research (MUR) through the National Recovery and Resilience Plan (PNRR) with the call *Young Researchers - Seal of Excellence* (CUP number: E13C22002920006).

Federica Cappelluti and Alberto Tibaldi (Politecnico di Torino) are gratefully acknowledged for their support and feedback concerning the original project proposal.

ORCID iD

Matteo Cagnoni 0000-0003-0599-1715

References

[1] Shockley W and Queisser H J 1961 Detailed balance limit of efficiency of *p-n* junction solar cells *J. Appl. Phys.* **32** 510–9
[2] Rühle S 2016 Tabulated values of the Shockley-Queisser limit for single junction solar cells *Sol. Energy* **130** 139–47
[3] Cristóbal López A B, Martí Vega A and López A L (eds) 2012 *Next Generation of Photovoltaics: New Concepts*, ed (Springer)
[4] A L López and S Hegedus 2011 *Handbook of Photovoltaic Science and Engineering* 2nd edn, ed (Wiley)
[5] Luque A and Martí A 1997 Increasing the efficiency of ideal solar cells by photon induced transitions at intermediate levels *Phys. Rev. Lett.* **78** 5014–7
[6] Luque A and Martí A 2010 The intermediate band solar cell: progress toward the realization of an attractive concept *Adv. Mater.* **22** 160–74
[7] Luque A and Martí A 2001 A metallic intermediate band high efficiency solar cell *Prog. Photovolt., Res. Appl.* **9** 73–86
[8] Okada Y *et al* 2015 Intermediate band solar cells: recent progress and future directions *Appl. Phys. Rev.* **2** 021302
[9] Oni A M, Mohsin A S M, Mosaddequr Rahman M D and Bhuian M B H 2024 A comprehensive evaluation of solar cell technologies, associated loss mechanisms and efficiency enhancement strategies for photovoltaic cells *Energy Rep.* **11** 3345–66
[10] Tanabe K, Guimard D, Bordel D and Arakawa Y 2012 High-efficiency InAs/GaAs quantum dot solar cells by metalorganic chemical vapor deposition *Appl. Phys. Lett.* **100** 193905
[11] Luque A, Martí A, Stanley C, López N, Cuadra L, Zhou D, Pearson J L and McKee A 2004 General equivalent circuit for intermediate band devices: potentials, currents and electroluminescence *J. Appl. Phys.* **96** 903–9
[12] Palacios P, Aguilera I, Sánchez K, Conesa J C and Wahnón P 2008 Transition-metal-substituted indium thiospinels as novel intermediate-band materials: prediction and understanding of their electronic properties *Phys. Rev. Lett.* **101** 046403
[13] Marsen B, Klemz S, Unold T and Schock H-W 2012 Investigation of the sub-bandgap photoresponse in $CuGaS_2$: Fe for intermediate band solar cells *Prog. Photovolt., Res. Appl.* **20** 625–9
[14] Levinshtein M, Rumyantsev S and Shur M 1996 *Handbook Series on Semiconductor Parameters* vol 1: Si, Ge, C (Diamond), GaAs, GaP, GaSb, InAs, InP, InSb (World scientific)
[15] Shockley W and Read W T 1952 Statistics of the recombinations of holes and electrons *Phys. Rev.* **87** 835–42
[16] Hall R N 1952 Electron-hole recombination in germanium *Phys. Rev.* **87** 387–387
[17] Luque A, Martí A and Stanley C 2012 Understanding intermediate-band solar cells *Nat. Photon.* **6** 146–52
[18] Luque A, Martí A, Antolín E and Tablero C 2006 Intermediate bands versus levels in non-radiative recombination *Physica B* **382** 320–7
[19] Mott N F 1968 Metal-insulator transition *Rev. Mod. Phys.* **40** 677–83
[20] Martí A *et al* 2013 Six not-so-easy pieces in intermediate band solar cell research *J. Photon. Energy* **3** 031299
[21] Shan W, Walukiewicz W, Ager J W, Haller E E, Geisz J F, Friedman D J, Olson J M and Kurtz S R 1999 Band anticrossing in GaInNAs alloys *Phys. Rev. Lett.* **82** 1221–4
[22] Walukiewicz W, Shan W, Yu K M, Ager J W, Haller E E, Miotkowski I, Seong M J, Alawadhi H and Ramdas A K 2000 Interaction of localized electronic states with the conduction band: band anticrossing in II-VI semiconductor ternaries *Phys. Rev. Lett.* **85** 1552–5
[23] López N, Reichertz L A, Yu K M, Campman K and Walukiewicz W 2011 Engineering the electronic band structure for multiband solar cells *Phys. Rev. Lett.* **106** 028701
[24] Tablero C and Wahnón P 2003 Analysis of metallic intermediate-band formation in photovoltaic materials *Appl. Phys. Lett.* **82** 151–3
[25] Padilha A C M, Raebiger H, Rocha A R and Dalpian G M 2016 Charge storage in oxygen deficient phases of TiO_2: defect physics without defects *Sci. Rep.* **6** 28871
[26] Rasukkannu M, Velauthapillai D and Vajeeston P 2017 Computational modeling of novel bulk materials for the intermediate-band solar cells *ACS Omega* **2** 1454–62
[27] Rasukkannu M, Velauthapillai D and Vajeeston P 2018 A first-principle study of the electronic, mechanical and optical properties of inorganic perovskite Cs_2SnI_6 for intermediate-band solar cells *Mater. Lett.* **218** 233–6
[28] Rasukkannu M, Velauthapillai D and Vajeeston P 2018 Hybrid density functional study of $Au_2Cs_2I_6$, Ag_2GeBaS_4, Ag_2ZnSnS_4, and $AgCuPO_4$ for the intermediate band solar cells *Energies* **11** 3457
[29] Liu Q, Cai Z, Han D and Chen S 2018 Natural intermediate band in $I_2 - II - IV - VI_4$ quaternary chalcogenide semiconductors *Sci. Rep.* **8** 1604
[30] Baquião D J and Dalpian G M 2019 Computational screening of bulk materials with intrinsic intermediate band *Comput. Mater. Sci.* **158** 382–8
[31] Curtarolo S *et al* 2012 AFLOWLIG.ORG: a distributed materials properties repository from high-throughput *phAb Initio* calculations *Comput. Mater. Sci.* **58** 227–35
[32] Ahluwalia G K (ed) 2017 *Applications of Chalcogenides: S, Se and Te*, ed (Springer)
[33] King R B 2006 *Encyclopedia of Inorganic Chemistry* (Wiley)
[34] Philipps S 2024 Photovoltaics report *Technical report* Fraunhofer ISE Freiburg, DE
[35] Das B, Aguilera I, Rau U and Kirchartz T 2020 What is a deep defect? Combining Shockley-Read-Hall statistics with multiphonon recombination theory *Phys. Rev. Mater.* **4** 024602
[36] Jain A *et al* 2013 Commentary: the Materials Project: a materials genome approach to accelerating materials innovation *APL Mater.* **1** 011002
[37] Ong S P, Richards W D, Jain A, Hautier G, Kocher M, Cholia S, Gunter D, Chevrier V L, Persson K A and Ceder G 2013 Python materials genomics (pymatgen): a robust, open-source python library for materials analysis *Comput. Mater. Sci.* **68** 314–9
[38] Munro J M, Latimer K, Horton M K, Dwaraknath S and Persson K A 2020 An improved symmetry-based approach to reciprocal space path selection in band structure calculations *npj Comput. Mater.* **6** 1–6
[39] Cagnoni M 2024 MADMAN: MAterial Data Mining and ANalysis (https://doi.org/10.5281/zenodo.14502853)
[40] Cagnoni M 2024 SCAMBIO: Solar Cell Analysis Made by Balancing photon Input and Output (https://doi.org/10.5281/zenodo.13950131)
[41] Virtanen P *et al* 2020 SciPy 1.0: fundamental algorithms for scientific computing in Python *Nat. Methods* **17** 261–72

[42] Viktor I F' 1969 *Heavily Doped Semiconductors* (Plenum Press)
[43] Liang W Y and Beal A R 1976 A study of the optical joint density-of-states function *J. Phys. C: Solid State Phys.* **9** 2823
[44] Fan X D, Peng J L and Bursill L A 1998 Joint density of states of wide-band-gap materials by electron energy loss spectroscopy *Mod. Phys. Lett. B* **12** 541–54
[45] O'Leary S K 2004 An empirical density of states and joint density of states analysis of hydrogenated amorphous silicon: a review *J. Mater. Sci., Mater. Electron.* **15** 401–10
[46] Levy M Y and Honsberg C 2009 Absorption coefficients of intermediate-band media *J. Appl. Phys.* **106** 073103
[47] Levy M Y and Honsberg C 2008 Intraband absorption in solar cells with an intermediate band *J. Appl. Phys.* **104** 113103
[48] Fox M 2010 *Optical Properties of Solids* 2nd edn (Oxford University Press)
[49] Strandberg R and Reenaas T W 2009 Photofilling of intermediate bands *J. Appl. Phys.* **105** 124512
[50] Levy M Y and Honsberg C 2008 Solar cell with an intermediate band of finite width *Phys. Rev. B* **78** 165122
[51] Würfel P 1982 The chemical potential of radiation *J. Phys. C: Solid State Phys.* **15** 3967–85
[52] Testa P, Cagnoni M and Cappelluti F 2024 Detailed-balance assessment of radiative cooling for multi-junction solar cells under unconcentrated and low-concentrated light *Sol. Energy Mater. Sol. Cells* **274** 112958
[53] Cagnoni M, Testa P, Dolado J S and Cappelluti F 2023 Extended detailed balance modeling toward solar cells with cement-based radiative coolers *Prog. Photovolt., Res. Appl.* **33** 54–63
[54] Richard M M 2020 *Electronic Structure: Basic Theory and Practical Methods* 2nd edn (Cambridge University Press)
[55] Blöchl P E 1994 Projector augmented-wave method *Phys. Rev. B* **50** 17953–79
[56] Larsen A H *et al* 2017 The atomic simulation environment - a Python library for working with atoms *J. Phys.: Condens. Matter* **29** 273002
[57] Jørgen Mortensen J *et al* 2024 GPAW: an open Python package for electronic structure calculations *J. Chem. Phys.* **160** 092503
[58] Perdew J P, Burke K and Ernzerhof M 1996 Generalized gradient approximation made simple *Phys. Rev. Lett.* **77** 3865–8
[59] Cagnoni M n.d. Detailed-balance efficiency limit of intermediate-band solar cells using crystalline chalcogenides from the Materials Project (in preparation) *Zenodo* (https://doi.org/10.5281/zenodo.14503029)
[60] Imada M, Fujimori A and Tokura Y 1998 Metal-insulator transitions *Rev. Mod. Phys.* **70** 1039–263
[61] Böttcher P 1980 Darstellung und Kristallstruktur der Dialkalimetalltrichalkogenide Rb_2S_3, Rb_2Se_3, Cs_2S_3 und Cs_2Se_3 *Z. fur Anorg. Allg. Chem.* **461** 13–21
[62] Zhou W Y, Meetsma A, de Boer J L and Wiegers G A 1992 Characterization and electrical transport properties of the misfit layer compounds $(BiSe)_{1.10}NbSe_2$ and $(BiSe)_{1.09}TaSe_2$ *Mater. Res. Bull.* **27** 563–72
[63] Petricek V, Cisarova I, de Boer J L, Zhou W, Meetsma A, Wiegers G A and van Smaalen S 1993 The modulated structure of the commensurate misfit-layer compound $(BiSe)_{1.09}TaSe_2$ *Acta Crystallogr. B* **49** 258–66
[64] Zhu H, Teale S, Lintangpradipto M N, Mahesh S, Chen B, McGehee M D, Sargent E H and Bakr O M 2023 Long-term operating stability in perovskite photovoltaics *Nat. Rev. Mater.* **8** 569–86
[65] Yu Y, Cagnoni M, Cojocaru-Mirédin O and Wuttig M 2019 Chalcogenide thermoelectrics empowered by an unconventional bonding mechanism *Adv. Funct. Mater.* **30** 1904862
[66] Tang G *et al* 2024 Interplay between metavalent bonds and dopant orbitals enables the design of SnTe thermoelectrics *Nat. Commun.* **15** 9133
[67] Mäckel H and MacKenzie R C I 2018 Determination of charge-carrier mobility in disordered thin-film solar cells as a function of current density *Phys. Rev. Appl.* **9** 034020
[68] Cappelluti F *et al* 2018 Light-trapping enhanced thin-film III-V quantum dot solar cells fabricated by epitaxial lift-off *Sol. Energy Mater. Sol. Cells* **181** 83–92
[69] Littlewood P B 1980 The crystal structure of IV-VI compounds. I. Classification and description *J. Phys. C: Solid State Phys.* **13** 4855–73
[70] Lencer D, Salinga M, Grabowski B, Hickel T, Neugebauer J and Wuttig M 2008 A map for phase-change materials *Nat. Mater.* **7** 972–7
[71] Esser M, Deringer V L, Wuttig M and Dronskowski R 2015 Orbital mixing in solids as a descriptor for materials mapping *Solid State Commun.* **203** 31–34
[72] Cagnoni M, Führen D and Wuttig M 2018 Thermoelectric performance of IV-VI compounds with octahedral-like coordination: a chemical-bonding perspective *Adv. Mater.* **30** 1801787
[73] Raty J-Y, Schumacher M, Golub P, Deringer V L, Gatti C and Wuttig M 2019 A quantum-mechanical map for bonding and properties in solids *Adv. Mater.* **31** 1806280
[74] Barbe J 1983 Convenient relations for the estimation of bond ionicity in A-B type compounds *J. Chem. Educ.* **60** 640
[75] Wei S, Lucas P and Angell C A 2019 Phase-change materials: the view from the liquid phase and the metallicity parameter *MRS Bull.* **44** 691–8
[76] Mulliken R S 1934 A new electroaffinity scale; together with data on valence states and on valence ionization potentials and electron affinities *J. Chem. Phys.* **2** 782–93
[77] European Chemical Society 2023 The 90 natural elements that make up everythings: how much is there? is that enough? is it sustainable? *Technical report* European Chemical Society Brussels, BE
[78] Mori-Sánchez P, Cohen A J and Yang W 2008 Localization and delocalization errors in density functional theory and implications for band-gap prediction *Phys. Rev. Lett.* **100** 146401
[79] Ullrich C A 2016 *Time-Dependent Density-Functional Theory: Concepts and Applications* (Oxford University Press)
[80] Crowley J M, Tahir-Kheli J and Goddard W A III 2016 Resolution of the band gap prediction problem for materials design *J. Phys. Chem. Lett.* **7** 1198–203